EFFICACY OF TARGETING BONE-SPECIFIC GIP RECEPTOR IN OVARIECTOMY-INDUCED BONE LOSS

Guillaume Mabilleau[1,2], Benoit Gobron[1,3], Aleksandra Mieczkowska[1], Rodolphe Perrot[4], Daniel Chappard[1,2,4]

[1] Groupe d'Etudes Remodelage Osseux et bioMatériaux, GEROM, SFR 42-08, Université d'Angers, IRIS-IBS Institut de Biologie en Santé, CHU d'Angers, 49933 Angers cedex - France.

[2] Bone pathology unit, Angers university hospital, 49933 Angers cedex –France

[3] Rheumatology department, Angers university hospital, 49933 Angers cedex-France

[4] Service Commun d'Imageries et d'analyses microscopiques, SCIAM, SFR 42-08, Université d'Angers, IRIS-IBS Institut de Biologie en Santé, CHU d'Angers, 49933 ANGERS Cedex - FRANCE

Please send all correspondence to:

Guillaume Mabilleau, PhD
GEROM-LHEA UPRES EA 4658
Institut de Biologie en Santé
Université d'Angers
4 rue larrey
49933 Angers Cedex 09
France

☎ : +33(0) 244 688 450
Fax : +33(0) 244 688 451
✉ : guillaume.mabilleau@univ-angers.fr

Running title: GIP in OVX-induced bone loss

Abstract word count: 230 words

Manuscript word count: 4,689 words

Keywords: GIP-Tag, GIP_{1-30}, bone loss, bone matrix composition, bone microarchitecture

LIST OF ABBREVIATIONS

5-FAM: 5 carboxy-fluorescein

αMEM: alpha minimum essential medium

AMPKα2: AMP activated protein kinase alpha 2

ANCOVA: Analysis of covariance

ANOVA: Analysis of variance

BM: Bone marrow

BSA: Bovine serum albumin

cAMP: cyclic adenosine monophosphate

CREB: cAMP response element-binding protein

Ct.Ar: cortical area

Ct.Th: Cortical thickness

CtB: Cortical bone

CTx-I:

DPP-4: Dipeptidylpeptidase-4

E_{IT}: Indentation modulus

FBS: Fetal bovine serum

FTIRM: Fourier transform infrared microspectroscopy

GIP: Glucose-dependent insulinotropic polypeptide

GIPr: Glucose-dependent insulinotropic polypeptide receptor

H_{IT}: Indentation hardness

Iap: Moment of inertia about the anteroposterior axis

Iml: Moment of inertia about the mediolateral axis

J: Polar moment of inertia

Ma.Ar: Marrow area

M-CSF: Macrophage-colony stimulating factor

MicroCT: X-ray microcomputed tomography

OVX: Ovariectomy

48 P1NP: N-terminal propeptide of type I procollagen

49 pHEMA: Poly(2-hydroxyethylmethacrylate)

50 pMMA: Poly(methylmethacrylate)

51 qBEI: Quantitative backscattered electron imaging

52 RANKL: Receptor activator of nuclear factor-kB ligand

53 STAT2: Signal transducer and activator of transcription 2

54 Tt.Ar: Total cross-sectional area

55 W_{plast}: Dissipated energy

ABSTRACT

Glucose-dependent insulinotropic polypeptide (GIP) has been recognized in the last decade as an important contributor of bone remodeling and is necessary for optimal bone quality. However, GIP receptors are expressed in several tissues in the body and little is known about the direct versus indirect effects of GIP on bone remodeling and quality. The aims of the present study were to validate two new GIP analogues, called [D-Ala^2]-GIP-Tag and [D-Ala^2]-GIP$_{1-30}$, that specifically target either bone or whole body GIP receptors, respectively; and to ascertain the beneficial effects of GIP therapy on bone in a mouse model of ovariectomy-induced bone loss. Both GIP analogues exhibited similar binding capacities at the GIP receptor and intracellular responses as full-length GIP$_{1-42}$. Furthermore, only [D-Ala^2]-GIP-Tag, but not [D-Ala^2]-GIP$_{1-30}$, was undoubtedly found exclusively in the bone matrix and released at acidic pH. In ovariectomized animals, [D-Ala^2]-GIP$_{1-30}$ but not [D-Ala^2]-GIP-Tag ameliorated bone stiffness at the same magnitude than alendronate treatment. Only [D-Ala^2]-GIP$_{1-30}$ treatment led to significant ameliorations in cortical microarchitecture. Although alendronate treatment increased the hardness of the bone matrix and the type B carbonate substitution in the hydroxyapatite crystals, none of the GIP analogues modified bone matrix composition. Interestingly, in ovariectomy-induced bone loss, [D-Ala²]-GIP-Tag failed to alter bone strength, microarchitecture and bone matrix composition. Overall, this study shows that the use of a GIP analogue that target whole body GIP receptors might be useful to improve bone strength in ovariectomized animals.

1. INTRODUCTION

Some evidences have emerged recently that the gut, and more specifically entero-endocrine cells, may play a role in maintaining optimal bone quality and bone mass (Gaudin-Audrain, et al. 2013; Henriksen, et al. 2003; Mabilleau, et al. 2013; Mieczkowska, et al. 2013; Mieczkowska, et al. 2015b; Nissen, et al. 2014; Torekov, et al. 2014; Tsukiyama, et al. 2006; Walsh and Henriksen 2010; Xie, et al. 2005). Among the plethora of peptides secreted by the gastrointestinal tract, the glucose-dependent insulinotropic polypeptide (GIP), synthesized and secreted by entero-endocrine K cells, has emerged as a potential candidate. Indeed, whole body GIP receptor (GIPr)-deficiency led to alterations of trabecular and cortical bone microarchitectures, tissue mineral density and collagen maturity (Gaudin-Audrain et al. 2013; Mieczkowska et al. 2013). Furthermore, administration of stable GIP analogues improved bone matrix composition and biomechanics at the tissue level in healthy and diabetic rodent models (Mabilleau, et al. 2014; Mansur, et al. 2015; Mansur, et al. 2016).

In rodents, the GIPr is widely expressed in the body and expression has been documented in the endocrine pancreas, gastro-intestinal tract, adipose tissue, adrenal cortex, pituitary gland, vascular endothelium and several regions in the central nervous system (Baggio and Drucker 2007). Expression in bone has also been reported and the GIPr seems to be expressed in rodent and human osteoblasts, osteocytes and osteoclasts (Bollag, et al. 2000; Mabilleau, et al. 2016; Mieczkowska, et al. 2015a). However, due to this wide variety of tissue expression, it is not clear whether the marked bone effects observed in previous rodent studies arise from inactivation/activation of bone-specific GIPr or extraskeletal GIPr.

The rapid degradation of GIP in plasma by dipeptidyl peptidase-4 (DPP-4) precludes to its use as a therapeutic approach. As such, a series of GIP modifications have previously been conducted and led to several GIP analogues with proven efficacy (Irwin and Flatt 2009). From these manipulations, it appears that the N-terminal extremity of GIP, and particularly the first two amino acids, was particularly important in allowing receptor activation. Furthermore, only the first 30 amino acids are required to induce biological activity

104 (Hinke, et al. 2001). As such, we produced two new GIP analogues, namely [D-Ala^2]-GIP$_{1-30}$
105 and [D-Ala^2]-GIP-Tag that possess a D-alanine in position 2 to confer DPP-4 resistance.
106 Furthermore, [D-Ala^2]-GIP-Tag possesses a tag of 9 negatively charged amino acids at its C-
107 terminal extremity that, according to previous published studies, should give a bone-specific
108 affinity (Kasugai, et al. 2000; Yokogawa, et al. 2001). The current gold standard medication
109 for treating post-menopausal osteoporosis is represented by bisphosphonates and as such,
110 we thought to also ascertain how the two new molecules above compared with alendronate.
111 The main goals of this study were to (1) verify that the tag confers a bone-specific
112 targeting, (2) ascertain the biological efficacy of these two new GIP analogues, [D-Ala^2]-GIP$_{1-}$
113 $_{30}$ and [D-Ala^2]-GIP-Tag and (3) investigate their therapeutic potentials in ovariectomy-
114 induced bone fragility as compared to alendronate.
115
116 **2. MATERIAL AND METHODS**
117 **2.1. Reagents**
118 All GIP analogues were purchased from GeneCust Europe with a purity >95% (Dudelange,
119 Luxembourg). Purity has been verified by high performance liquid chromatography and
120 peptide composition validated by mass spectroscopy. Sequences are provided in table 1.
121 Macrophage-colony stimulating factor (M-CSF) and receptor activator of nuclear factor kB
122 ligand (RANKL) were purchased from R&D Systems Europe (Abingdon, UK). Fluo-4AM was
123 purchased from Invitrogen (Carlsbad, CA, USA). All other chemicals were obtained from
124 Sigma-Aldrich (Lyon, France) unless otherwise stated.
125
126 **2.2. In vitro mineral binding assay**
127 Carboxymethylated poly(2-hydroxyethylmethacrylate) (pHEMA) disks and their mineralization
128 were performed as previously described (Filmon, et al. 2002). Mineralized disks were
129 incubated for 16 h with 5 nmoles of 5-carboxyfluorescein (5-FAM), 5-FAM-[D-Ala^2]-GIP$_{1-30}$, 5-
130 FAM-[D-Ala^2]-GIP-Tag or calcein green. PHEMA disks were rinsed extensively with distilled
131 water prior to observation with a Leica TCS SP8 confocal laser scanning microscope (Leica,

Nanterre, France). Excitation was performed at 488 nm with an argon laser and emission was recorded in the range 510-550 nm. After observation, the mineral was dissolved with 0.2M HCl overnight and fluorescence readings were performed with a M2 microplate reader (Molecular devices, St Gregoire, France) set up at 480 nm for excitation and 530 nm for emission. Calcium concentrations were estimated as published previously (Degeratu, et al. 2013).

2.3. Cell culture and activity of GIP analogues

MC3T3-E1 cells were purchased from American type culture collection (ATCC, Teddington, UK). Cells were grown and expanded in propagation medium containing alpha minimum essential medium (αMEM) supplemented with 5% fetal bovine serum (FBS), 5% bovine calf serum, 100 U/mL penicillin, and 100 µg/mL streptomycin in a humidified atmosphere enriched with 5% CO_2 at 37°C.

Competitive whole cell binding studies were performed in cold αMEM supplemented with 0.1% bovine serum albumin (BSA), protease inhibitors (Halt protease inhibitor cocktail, Thermofisher scientific, Villebon sur Yvette, France), 8 x 10^{-9}M FAM-GIP_{1-42}, and appropriate peptide concentrations. Equilibrium binding was achieved overnight at 4°C. Cells were then washed twice with cold assay buffer, solubilized in 0.1M NaOH, and transferred to opaque microplate for fluorescence readings.

Cyclic adenosine monophosphate (cAMP) stimulation experiment was performed in response to 100 pM GIP analogues in MC3T3-E1 cells with a fluorometric commercially available kit (reference KGE002B, R&D Systems Europe) (Mieczkowska et al. 2015a). Assessment of the cell phospho-proteome was assessed with the Proteome profiler anti-phosphokinase assay (reference ARY003b, R&D Systems Europe).

MC3T3-E1 cells were seeded in 96-well plate with clear bottom and opaque edges (ibidi GmbH, Martinsried, Germany). Cells were incubated with 4 µM Fluo-4-AM for 45 min at 37°C in the dark and washed with pre-warmed HEPES buffered saline. The plate was placed in a M2 microplate reader (Molecular devices) and signals were acquired at 37°C with an

160 excitation wavelength of 490 nm and an emission wavelength set at 515 nm for 5 min. Cells
161 were then stimulated with 100 pM GIP analogues for 15 min and signals were again acquired
162 with the microplate reader. Autofluorescence was measured in unloaded cells, and this value
163 was subtracted from all measurements.
164 Collagen maturity assay was performed as described in detail elsewhere (Mieczkowska et al.
165 2015a).
166 In order to generate mature human osteoclasts, peripheral mononuclear blood cells were
167 isolated from buffy coat (Etablissement français du sang, Angers, France) and cultured in the
168 presence of 25 ng/ml M-CSF and 30 ng/ml soluble human RANKL as described previously
169 (Mabilleau, et al. 2011).
170

171 **2.4 Animals**

172 BALB/c (BALB/cJRj) mice were obtained from Janvier Labs (Saint-Berthevin, France). All
173 animal experiments were approved by Ethical committee in animal use of the Pays de la
174 Loire under the animal license CEEA-PdL06-01740.01. Mice were housed 4 animals per
175 cage in the institutional animal lab (Agreement E49007002) at 24°C +/- 2°C with a 12-hour
176 light/dark cycle, and were provided with tap water and normal diet (Diet A04, Safe, Augy,
177 France) *ad libitum* until sacrifice by cervical dislocation. All procedures were conducted
178 according to the French Animal Scientific Procedures Act 2013-118.
179

180 **2.5. *In vivo* localization of fluorescently labelled GIP analogues**

181 Intraperitoneal injections of saline or fluorescent GIP analogues (50 nmoles/kg body weight)
182 were performed at 4 weeks of age in 15 female BALB/c mice (n=5/group). This dose of
183 fluorescent GIP analogues was chosen to ensure detection in the investigated tissues.
184 Twenty-four hours after injection, visceral adipose tissue, adrenal gland, bladder, left femur
185 and tibia, brain, heart, small intestine, kidney, liver, lung, pancreas, skeletal muscle, spleen
186 and stomach were collected, immediately snap-frozen in liquid nitrogen and stored at -80°C
187 until use. Then, frozen tissues were powdered, suspended in Tris 0.1M pH 7.4 and

fluorescence readings with a microplate reader as detailed above were performed. Fluorescence readings were normalized by the concentration of proteins measured with the bicinchoninic acid assay (Pierce Biotechnology, Rockford, IL). Right femurs of 4-week-old mice were collected at necropsy, fixed in buffered formalin and embedded in polymethylmethacrylate (pMMA) at low temperature (Chappard 2009). Thick cross-sections at the mid-diaphysis of all femurs were cut with a low speed precision saw (Minitom, Struers, Champigny sur Marne, France). Femur sections were grinded up to a thickness of 50 µm and subsequently imaged with the confocal microscope as explained above.

Additionally, right tibias of 5-FAM-[D-Ala^2]-GIP-Tag-injected mice were collected at necropsy, fixed in buffered formalin and embedded in polymethylmethacrylate (pMMA) at low temperature. Thick cross-sections (500 µm-thick) at the mid-diaphysis were cut with a low speed precision saw and incubated in saline or 0.1M acetic acid (pH 4.5) for 24 h. The resulting solution was buffered with 1M Tris and fluorescence readings were performed with the M2 microplate reader as explained above.

2.6. Long term effects of GIP analogues in ovariectomy-induced bone loss

Bilateral ovariectomy (OVX) was performed in 32 BALB/c mice at 12 weeks of age under general anesthesia supplemented with a β2 adrenergic receptor agonist. At 16 weeks of age, mice were randomly allocated into four groups: vehicle daily (OVX+Veh, n=8), 25 nmoles/kg/day intraperitoneally (ip) [D-Ala^2]-GIP$_{1-30}$ (OVX+GIP$_{1-30}$, n=8), 25 nmoles/kg/day ip [D-Ala^2]-GIP-Tag (OVX+GIP-Tag, n=8) and 10 µg/kg alendronate twice a week ip (OVX+Aln, n=8). These doses and regimens of GIP analogues and alendronate were based on previous published studies where these molecules were proven active with beneficial effects on bone or equivalent to approved clinical dose (Mabilleau et al. 2014; Shao, et al. 2017). Eight sham-operated female BALB/c mice with the same age and injected daily with saline were used as controls (Sham+Veh). All mice from the second study were also administered with calcein (10 mg/kg; ip) 10 and 2 days before being culled at 24 weeks of age. At necropsy, blood was collected by intracardiac aspiration (~250µl). Non-fasting glucose level were evaluated with

an Accu-Chek® mobile glucometer (Roche Diabetes Care GmbH, Mannheim, Germany). Then blood were spun at 13,000 rpm for 15 min at 4°C and serum was aliquoted, snap-frozen in liquid nitrogen and stored at -80°C until use. After necropsy, tibias, femurs and uterus were collected and cleaned of soft tissues. Femur length was measured with a digital caliper (Mitutoyo, Roissy en France, France).

2.7. ELISA

Serum levels of C-terminal telopeptide of collagen type I (CTx-I) and N-terminal propeptide of type I collagen (P1NP) were measured with the RatLaps and Rat/mouse P1NP ELISA kits, respectively (Immunodiagnostic Systems Ltd, Boldon, UK), according to the manufacturer recommendations.

2.8. Microcomputed tomography

X-ray microcomputed tomography (MicroCT) analyses of the abdomen were performed to measure abdominal fat volume, that represents a good indicator of whole body fat mass (Judex, et al. 2010). Anesthetized animals were placed in a Skyscan 1076 microtomograph (Bruker MicroCT, Kontich, Belgium) and the region localized between L1 and the hip was selected for fat depot evaluation. Acquisitions were performed at 40 kV, 250 µA, 100-ms integration time. The isotropic pixel size was fixed at 35 µm, the rotation step at 0.6° and exposure was done with a 0.5-mm aluminum filter. Tibias were scanned with a Skyscan 1172 microtomograph (Bruker MicroCT) operated at 70 kV, 100 µA, 340-ms integration time. The isotropic pixel size was fixed at 4 µm, the rotation step at 0.25° and exposure was done with a 0.5-mm aluminium filter. Each 3D reconstruction image dataset was binarized using global thresholding. Cortical volume of interest extended on 1-mm centered at the midshaft tibia. All histomorphometrical parameters were determined according to guidelines and nomenclature proposed by the American Society for Bone and Mineral Research (Bouxsein, et al. 2010).

2.9. Marrow adipose tissue assessment

After microCT scans, tibias were embedded undecalcified in pMMA at 4°C. Longitudinal sections were cut and stained with toluidine blue. The extent of marrow adipose tissue (Ad.Ar/Ma.Ar) was computerized with a routine in Image J (release 1.51s, National Institutes of Health, Bethesda, MA). The nomenclature proposed by the American Society for Bone and Mineral Research was used in this study (Dempster, et al. 2013).

2.10. Bone strength assessment

At necropsy, femurs were cleaned of soft tissue and immediately frozen in a saline-soaked gauze at -20°C. Three-point bending experiments were performed on femurs after thawing bones at 4°C overnight. Measurements were done with an Instron 5942 (Instron, Elancourt, France) as reported previously (Mieczkowska et al. 2015b). The load-displacement curve was acquired with the Bluehill 3 software (Instron). Ultimate load, ultimate displacement, stiffness and total absorbed energy were computerized (Turner and Burr 1993).

After three-point bending experiments, femurs were embedded undecalcified in pMMA at 4°C and cross-sections were made at the midshaft using a diamond saw (Accutom, Struers, Champigny sur Marne, France). Blocks were polished to a 1-µm finish with diamond particles (Struers, France) and subjected to rehydration in saline 24h prior to nanoindentation testing. Twelve indentations, at distance from canals, osteocyte lacunae and/or microcracks were randomly positioned in cortical bone with a NHT-TTX system (Anton Paar, Les Ulis, France) as previously detailed (Aguado, et al. 2017). At maximum load, a holding period of 15 seconds was applied to avoid creeping of the bone material. The following material properties at the tissue-level: maximum load (Force max), indentation modulus (E_{IT}), indentation hardness (H_{IT}) and dissipated energy (W_{plast}), were determined according to Oliver and Pharr (Oliver and Pharr 1992).

2.11. Fourier-transform infrared microscopy (FTIRM)

Four micrometers cross-sectional sections of the midshaft femur were sandwiched between BaF_2 optical windows and FTIRM assessment was performed at bone formation site by

recording infrared spectra only between double calcein labeling. A Bruker Vertex 70 spectrometer (Bruker optics, Ettlingen, Germany) interfaced with a Bruker Hyperion 3000 infrared microscope were used as previously reported (Pereira, et al. 2017). Each spectrum was corrected for Mie scattering with the RMieS-EMSC_v5 algorithm (kind gift of Prof Peter Gardner, University of Manchester, UK) prior to be subjected to pMMA subtraction. Second derivative spectroscopy was applied to find the position of underlying peaks and curve fitting was performed with a routine script in Matlab (The Mathworks, Natick, USA) as previously reported (Mansur et al. 2015). The evaluated infrared spectral parameters were (1) mineral-to-matrix ratio, calculated as the ratio of integrated areas of the υ1, υ3 phosphate band at 900-1200 cm^{-1} to the amide I band at 1585-1725 cm^{-1} (Boskey, et al. 2005); (2) mineral maturity calculated as the area ratio of the subbands at 1020 cm^{-1} and 1030 cm^{-1} of the phosphate band (Gadaleta, et al. 1996); (3) carbonate-to-phosphate ratio, calculated as the ratio of the υ2 carbonate band at 850-900 cm^{-1} to the υ1,υ3 phosphate band (Paschalis, et al. 1996); (4) carbonate substitution type by integrating the area of subbands located at 866 cm^{-1} (labile), 871 cm^{-1} (type B) and 878 cm^{-1} (type A) over the υ2 carbonate band (Rey, et al. 1989); (5) acid phosphate content, calculated as the area ratio of the 1127 cm^{-1} and 1096 cm^{-1} subbands (Spevak, et al. 2013) and (6) collagen maturity, determined as the relative ratio of subbands located at 1660 cm^{-1} (trivalent cross-links) and 1690 cm^{-1} (divalent cross-links) of the amide I peak (Paschalis, et al. 2001) .

2.12. Bone mineral density distribution (BMDD) evaluation

Quantitative backscattered electron imaging (qBEI) experiments were performed on the same blocks and same regions as nanoindentation. A full description of qBEI preparation, calibration and analysis has already been extensively described elsewhere (Mabilleau et al. 2013; Mieczkowska et al. 2015b; Roschger, et al. 1998). Cortical bone area was imaged at a 200 X nominal magnification, corresponding to a pixel size of 0.5 µm. Four images per samples were taken. Two variables were obtained from the bone mineral density distribution:

299 Ca_{mean} as the average calcium concentration and Ca_{width} as the width of the histogram at half
300 maximum of the peak. Following this, the blocks were imaged at a 200 X magnification with a
301 confocal microscope (Leica SP8, Leica, Nanterre, France) equipped with an argon laser at
302 488 nm and a hybrid GaAs detector (Leica) to find bone surface with double labels. Confocal
303 images were superimposed on qBEI images in order to delineate new bone matrix formed
304 during the time-course of the study. Using ImageJ 1.51s, a straight line (4 pixel width)
305 perpendicular to the mineralization front across the new bone structural unit with a step size
306 of 0.5µm was drawn on qBEI image. The calcium content was plotted *vs.* distance of
307 mineralization front. These plots show a biphasic aspect with fast mineralization process
308 close to the mineralization front followed by a slow mineralization process. The two
309 mineralization processes were then analysed by linear curve fitting with a lab-made routine in
310 Excel 2010 (Microsoft, Issy-les-Moulineaux, France). Ca_{turn} was determined as the calcium
311 concentration where the fast mineralization process was changing to the slow mineralization
312 process as described by Roschger et al.,(Roschger, et al. 2008)
313
314 **2.13. Statistical analysis**
315 All data were analyzed using Prism 6.0 (GraphPad Software Inc., La Jolla, CA). Mineral
316 binding was analyzed by a one-way analysis of variance (ANOVA) followed by *post hoc*
317 Dunnett's multiple comparisons tests. Tissue distribution of both fluorescent analogues was
318 analyzed by a two-way ANOVA with Sidak's multiple comparisons tests. GIPr binding assay
319 was analyzed by non-linear regression analysis. Intracellular signaling (cAMP, intracellular
320 calcium and phospho-proteins) as well as in vitro collagen maturity and extent of osteoclast
321 formation and resorption in vitro were analyzed with the non-parametrical Kruskal-Wallis test.
322 Due to the adaptive nature of bone, bone strength, bone microarchitecture and bone
323 compositional parameters have been adjusted for body size (body mass x femur length)
324 using a linear regression method as reported in details elsewhere (Jepsen, et al. 2015). One-
325 way ANOVA followed by *post hoc* Dunnett's multiple comparisons tests were employed to
326 analyze differences between OVX+Veh and all the other groups of mice in any of the body

size-adjusted parameters. Differences at p equal to or less than 0.05 were considered significant.

3. RESULTS

3.1. [D-Ala^2]-GIP-Tag but not [D-Ala^2]-GIP$_{1-30}$ is capable of binding to hydroxyapatite and targeting bone tissue

Microscopic examinations of calcospherites grown at the surface of carboxymethylated pHEMA revealed that 5-FAM-[D-Ala^2]-GIP-Tag and calcein green, but neither 5-FAM-[D-Ala^2]-GIP$_{1-30}$ nor 5-FAM alone, were significantly bound to hydroxyapatite (Figure 1A). Tissue distribution of the two fluorescently labeled analogues highlighted differences between the two molecules. Indeed, 5-FAM-[D-Ala^2]-GIP$_{1-30}$ was mainly observed in adipose tissue, adrenal gland, bone, brain, intestine, liver and pancreas, whilst 5-FAM-[D-Ala^2]-GIP-Tag was exclusively found in bone (Figure 1B). Microscopic examinations of femur midshaft cross-sections in 5-FAM-[D-Ala^2]-GIP-Tag-injected mice revealed the presence of fluorescent bands, suggesting the incorporation of this analogue in the bone mineral (Figure 1C). On the other hand, such bone distribution was not observed in 5-FAM-[D-Ala^2]-GIP$_{1-30}$-injected animals (Figure 1C). Furthermore, incubation of thick tibia slices in acidic conditions (pH 4.5), but not in neutral solution, was capable of releasing 5-FAM-[D-Ala^2]-GIP-Tag (Figure 1D).

3.2. Cellular and molecular activities of [D-Ala^2]-GIP-Tag are not affected by the C-terminal modification

Next, we thought to investigate the biological activity of both GIP analogues. As represented in Figure 2A, [D-Ala^2]-GIP$_{1-30}$ and [D-Ala^2]-GIP-Tag did not show any differences in their capacity to bind to the GIPr with IC50 of 65.5±2.5 pM and 72.9±2.7 pM, respectively. More importantly, their binding activity was similar to GIP$_{1-42}$, with IC 50 of 65.3±1.7 pM. Both GIP analogues were capable of inducing cAMP production and rise in intracellular calcium to the same level as observed with GIP$_{1-42}$ (Figure 2A). Phospho-proteome analysis showed that

355 osteoblasts stimulated with GIP_{1-42} also activated p38α, CREB, AMPKα2 and STAT2 in
356 addition to cAMP (Figure 2B). [D-Ala^2]-GIP_{1-30} and [D-Ala^2]-GIP-Tag showed similar actions
357 on all these intracellular pathways (Figure 2B). Finally, we tested whether [D-Ala^2]-GIP_{1-30}
358 and [D-Ala^2]-GIP-Tag were capable of improving collagen maturity as observed with GIP_{1-42}
359 and indeed, this parameter was significantly augmented by 32% and 37%, with [D-Ala^2]-GIP_{1-}
360 $_{30}$ and [D-Ala^2]-GIP-Tag, respectively as compared with untreated cells (Figure 2C). As
361 suspected, both GIP analogues were also capable to reduce osteoclast formation and
362 osteoclast-mediated bone resorption *in vitro* in a similar extent to GIP_{1-42} (Figure 2D).
363
364 **3.3. Effects of [D-Ala^2]-GIP_{1-30} vs. [D-Ala^2]-GIP-Tag in OVX-induced bone loss**
365 We next examined the biological effects of GIP analogues in the OVX mouse model. As
366 compared with Sham+Veh animals and shown in Table 2, OVX+Veh mice presented with
367 higher abdominal fat volume and CTx-I levels and lower uterus mass. Treatment with [D-
368 Ala^2]-GIP_{1-30} significantly reduced CTx-I levels whilst treatment of OVX animals with [D-Ala^2]-
369 GIP-Tag significantly reduced abdominal fat volume, marrow adipose tissue and CTx-I
370 levels. Alendronate administration only significantly reduced CTx-I levels.
371 After the 8-week experimental treatment period, structural mechanical properties were
372 assessed by three-point bending (Figures 3 A-F). As expected, OVX+Veh mice presented
373 with significant reductions in ultimate force (-18%, $p=0.0005$), yield load (-27%, $p<0.0001$)
374 and stiffness (-34%, $p<0.0001$). Treatments with alendronate or [D-Ala^2]-GIP_{1-30}, but not [D-
375 Ala^2]-GIP-Tag, significantly augmented by 33% ($p<0.0001$) and 25% ($p=0.0013$) stiffness,
376 respectively. Bone strength was also investigated at the tissue level by nanoindentation
377 (Figures 3 G-J). As compared with Sham animals, OVX+Veh mice presented no significant
378 alterations in any of the studied parameters. The use of alendronate significantly augmented
379 H_{IT} by 29% ($p=0.0191$). Neither [D-Ala^2]-GIP_{1-30} nor [D-Ala^2]-GIP-Tag significantly modified
380 strength at the tissue level.
381 As compared with Sham+Veh animals, significant microarchitectural alterations of cortical
382 bone were evidenced as expected in OVX+Veh animals and represented by lower total

cross-sectional area (Tt.Ar, -10%, p=0.0249), marrow area (Ma.Ar, -14%, p=0.0046) and cortical area (Ct.Ar, -9%, p=0.0248) (Table 3). On the other hand, cortical thickness (Ct.Th), moment of inertia about the anteroposterior (I_{ap}) or mediolateral (I_{ml}) axis and polar moment of inertia (J) were not significantly different between the two groups of animals. As compared with OVX+Veh animals, treatment with [D-Ala^2]-GIP$_{1-30}$ significantly increased Tt.Ar, Ma.Ar, Ct.Ar and J by 10% (p=0.0417), 16% (p=0.0041), 9% (p=0.0430) and 18% (p=0.0246), respectively. Treatment with [D-Ala^2]-GIP-Tag did not result in significant modifications of cortical microarchitecture although a trend to similar effects as observed with [D-Ala^2]-GIP$_{1-30}$ was noted (Table 3). Treatment with alendronate resulted only in lower values for I_{ml} (-21%, p=0.0277).

Alterations of bone matrix composition was also evidenced in OVX+Veh animals as compared with Sham+Veh (Figure 4). Indeed, at site of bone formation, collagen maturity and mineral-to-matrix ratio were significantly lowered by 25% (p=0.0261) and 35% (p=0.0070), respectively in OVX+Veh animals. As compared with OVX+Veh animals, treatment with [D-Ala^2]-GIP$_{1-30}$ or [D-Ala^2]-GIP-Tag significantly lowered the overall mean calcium distribution in the bone matrix (Ca_{mean}) by 7% (p=0.0002) and 4% (p=0.0217), respectively. These two molecules also reduced the Ca_{turn} value by 6% (p=0.005) and 7% (p=0.002), respectively. At site of bone formation, none of these molecules modified the bone matrix composition. On the other hand, treatment with alendronate significantly reduced calcium distribution heterogeneity (Ca_{width}) by 11% (p=0.0044) and augmented Ca_{turn} values by 7% (p<0.001) in the bone matrix. At site of bone formation, alendronate resulted in higher carbonate-to-phosphate ratio by 16% (p=0.0204), mainly by reduction in loosely bound carbonate (-47%, p=0.0053) and increase in type B carbonate substitution (31%, p=0.0008).

4. DISCUSSION

With respect to its important role in maintaining bone strength in animal models of receptor deletion, GIP has promises as a therapeutic agent in treating bone fragility. In the present study, we investigated bone-targeting capacities and biological activities as well as

411 therapeutical potencies of two new GIP analogues in ovariectomy-induced bone loss. The
412 bone-targeting capacity of [D-Ala^2]-GIP-Tag, as opposed to [D-Ala^2]-GIP$_{1-30}$, was evident and
413 emphasized the importance of acidic amino acids in promoting bone affinity. Acidic amino
414 acid tag mimics the observed aspartic acid repetition in the noncollagenous bone protein
415 osteopontin. In bone, after secretion, osteopontin rapidly binds to hydroxyapatite and
416 sequence analysis of osteopontin identified the aspartic acid repetition as a putative mineral-
417 binding site (Butler 1989; Oldberg, et al. 1986). Similarly to what is observed with
418 bisphosphonate, a molecule bound to the bone mineral is thought to be released upon bone
419 resorption. The first evidence suggesting such properties of the acidic amino acid tag was
420 reported by Kasugai and coworkers in 2000 (Kasugai et al. 2000). Since their discovery, at
421 least six distinct molecules have been developed so far with bone-targeting properties using
422 an acidic amino acid tag (Hsieh, et al. 2014; Miller, et al. 2008; Montano, et al. 2008;
423 Nishioka, et al. 2006; Takahashi, et al. 2008; Yokogawa et al. 2001). In 2007, Murphy et al.
424 reported the higher efficacy of acidic amino acid tags in comparison to the bisphosphonate
425 structural group (Murphy, et al. 2007). We deliberately chose to fuse this tag at the C-
426 terminal end of [D-Ala^2]-GIP$_{1-30}$ because only the first 30 amino acids are important for GIP
427 helicoïdal secondary structure and hence its receptor binding and biological properties
428 (Alana, et al. 2006; Manhart, et al. 2003). However, in this study, we also provided clear
429 evidences that [D-Ala^2]-GIP$_{1-30}$ and [D-Ala^2]-GIP-Tag presented the same receptor binding
430 affinities as full length GIP$_{1-42}$ and that the same intracellular signaling pathways were
431 activated in osteoblasts in response to these GIP analogues. Previously GIP$_{1-42}$ has been
432 reported to enhance collagen maturity in osteoblast cultures (Mieczkowska et al. 2015a) and
433 to reduce cell differentiation and activity in osteoclast cultures (Mabilleau et al. 2016). In the
434 present study, we provided clear evidences that the two new GIP analogues, [D-Ala^2]-GIP$_{1-30}$
435 and [D-Ala^2]-GIP-Tag, exhibited similar actions in osteoblast and osteoclast cultures.
436 However, when administered *in vivo*, these two molecules presented differences. Indeed, [D-
437 Ala^2]-GIP$_{1-30}$ localizes in several tissues that could potentially affect bone physiology whilst as
438 discussed above, [D-Ala^2]-GIP-Tag localizes almost exclusively in bone. In the ovariectomy-

induced bone fragility model, [D-Ala^2]-GIP$_{1-30}$, but not [D-Ala^2]GIP-Tag, was proven potent to improve bone strength, mainly by modifying the cortical microarchitecture. However, caution should be taken for interpretation of these observations. Firstly, the activity of [D-Ala²]-GIP-Tag has been tested in isolated cell culture, but not in vivo after incorporation into the bone mineral. Our release assay demonstrated that at acidic pH, close to pH obtained during osteoclast resorption, the fluorescent peptide could be released from bone. However, it was not possible to assess its biological activity. Furthermore, due to the low concentration given to the animals, it was not possible to assess the presence of [D-Ala²]-GIP-Tag in blood or urine. As such, we cannot rule out that the observed lack of effects of [D-Ala²]-GIP-Tag could be due to either low bioavailability or degradation of the peptide after osteoclast resorption. Another explanation, and in addition to GIPr tissue targeting, could suggest that to be beneficial for bone health, extraskeletal GIPr have to be targeted rather than bone-specific GIPr. However, a limitation to this study is that we did not generate tissue-specific invalidation or extraskeletal tissue specific activation of GIPr to ascertain how the GIP/GIPr pathway controls bone physiology.

The mechanism of action of [D-Ala^2]-GIP$_{1-30}$ was also compared with alendronate. In the present study, alendronate, given at a dose comparable to what is used in humans in the treatment of post-menopausal osteoporosis (i.e. 70 mg/week orally), improved bone strength by acting mostly on bone matrix composition (H_{IT}, Ca_{width}, carbonate-to-phosphate ratio) rather than restoring cortical bone microarchitecture. On the other hand, [D-Ala^2]-GIP$_{1-30}$ acted preferentially on cortical bone microarchitecture and had almost no action on bone matrix composition, except a small decrease in tissue mineral density. This indicates that the molecular mechanisms of action of these two pharmacological interventions are probably different and in the future, administration of both molecules jointly should be envisaged.

In conclusion, we developed two new GIP analogues that target whole-body GIPr or only bone-specific GIPr. In ovariectomized animals, only [D-Ala^2]-GIP$_{1-30}$ was potent in ameliorating bone strength by restoring cortical bone microarchitecture rather than acting on bone matrix composition in opposition to what was observed with alendronate. This study

brought new evidences that targeting the GIP/GIPr pathway might be valuable in bone disorders although further studies will be needed before translating these findings to human post-menopausal osteoporosis.

5. DECLARATION OF INTEREST

None of the authors has any conflict of interest to report

6. FUNDING

This work was supported by a grant from the Société Française de Rhumatologie.

7. AUTHOR CONTRIBUTIONS

Guillaume Mabilleau: Conception and Design, acquisition of data, analysis and interpretation of data, drafting and revising the manuscript

Benoit Gobron: acquisition of data, analysis and interpretation of data, revising the manuscript

Aleksandra Mieczkowska: acquisition of data, analysis and interpretation of data, revising the manuscript

Rodolphe Perrot: acquisition of data, analysis and interpretation of data, revising the manuscript

Daniel Chappard: Analysis and interpretation of data, revising the manuscript

All authors approved the current version of the manuscript. Guillaume Mabilleau takes responsibility for the integrity of the data and analysis.

8. ACKNOWLEDGEMENTS

The authors are grateful to Nadine Gaborit and Stéphanie Lemière for their help with microCT. The authors also thank the personnel of the animal care facility (University of Angers-SCAHU) for their help with animal handling and injection.

9. REFERENCES

Aguado E, Mabilleau G, Goyenvalle E & Chappard D 2017 Hypodynamia Alters Bone Quality and Trabecular Microarchitecture. *Calcif Tissue Int* **100** 332-340.

Alana I, Parker JC, Gault VA, Flatt PR, O'Harte FP, Malthouse JP & Hewage CM 2006 NMR and alanine scan studies of glucose-dependent insulinotropic polypeptide in water. *J Biol Chem* **281** 16370-16376.

Baggio LL & Drucker DJ 2007 Biology of incretins: GLP-1 and GIP. *Gastroenterology* **132** 2131-2157.

Bollag RJ, Zhong Q, Phillips P, Min L, Zhong L, Cameron R, Mulloy AL, Rasmussen H, Qin F, Ding KH, et al. 2000 Osteoblast-derived cells express functional glucose-dependent insulinotropic peptide receptors. *Endocrinology* **141** 1228-1235.

Boskey AL, DiCarlo E, Paschalis E, West P & Mendelsohn R 2005 Comparison of mineral quality and quantity in iliac crest biopsies from high- and low-turnover osteoporosis: an FT-IR microspectroscopic investigation. *Osteoporos Int* **16** 2031-2038.

Bouxsein ML, Boyd SK, Christiansen BA, Guldberg RE, Jepsen KJ & Muller R 2010 Guidelines for assessment of bone microstructure in rodents using micro-computed tomography. *J Bone Miner Res* **25** 1468-1486.

Butler WT 1989 The nature and significance of osteopontin. *Connect Tissue Res* **23** 123-136.

Chappard D 2009 Technical aspects: how do we best prepare bone samples for proper histological analysis? In *Bone cancer: progression and therapeutic approaches*, pp 203-210. Ed D Heymann. London: Academic press Elsevier.

Degeratu CN, Mabilleau G, Cincu C & Chappard D 2013 Aluminum inhibits the growth of hydroxyapatite crystals developed on a biomimetic methacrylic polymer. *J Trace Elem Med Biol* **27** 346-351.

Dempster DW, Compston JE, Drezner MK, Glorieux FH, Kanis JA, Malluche H, Meunier PJ, Ott SM, Recker RR & Parfitt AM 2013 Standardized nomenclature, symbols, and units for

522 bone histomorphometry: a 2012 update of the report of the ASBMR Histomorphometry
523 Nomenclature Committee. *J Bone Miner Res* **28** 2-17.
524 Filmon R, Grizon F, Basle MF & Chappaard D 2002 Effects of negatively charged groups
525 (carboxymethyl) on the calcification of poly(2-hydroxyethyl methacrylate). *Biomaterials* **23**
526 3053-3059.
527 Gadaleta SJ, Paschalis EP, Betts F, Mendelsohn R & Boskey AL 1996 Fourier transform
528 infrared spectroscopy of the solution-mediated conversion of amorphous calcium phosphate
529 to hydroxyapatite: new correlations between X-ray diffraction and infrared data. *Calcif Tissue*
530 *Int* **58** 9-16.
531 Gaudin-Audrain C, Irwin N, Mansur S, Flatt PR, Thorens B, Basle M, Chappard D &
532 Mabilleau G 2013 Glucose-dependent insulinotropic polypeptide receptor deficiency leads to
533 modifications of trabecular bone volume and quality in mice. *Bone* **53** 221-230.
534 Henriksen DB, Alexandersen P, Bjarnason NH, Vilsboll T, Hartmann B, Henriksen EE,
535 Byrjalsen I, Krarup T, Holst JJ & Christiansen C 2003 Role of gastrointestinal hormones in
536 postprandial reduction of bone resorption. *J Bone Miner Res* **18** 2180-2189.
537 Hinke SA, Manhart S, Pamir N, Demuth H, R WG, Pederson RA & McIntosh CH 2001
538 Identification of a bioactive domain in the amino-terminus of glucose-dependent
539 insulinotropic polypeptide (GIP). *Biochim Biophys Acta* **1547** 143-155.
540 Hsieh KC, Kao CL, Feng CW, Wen ZH, Chang HF, Chuang SC, Wang GJ, Ho ML, Wu SM,
541 Chang JK, et al. 2014 A novel anabolic agent: a simvastatin analogue without HMG-CoA
542 reductase inhibitory activity. *Org Lett* **16** 4376-4379.
543 Irwin N & Flatt PR 2009 Therapeutic potential for GIP receptor agonists and antagonists.
544 *Best Pract Res Clin Endocrinol Metab* **23** 499-512.
545 Jepsen KJ, Silva MJ, Vashishth D, Guo XE & van der Meulen MC 2015 Establishing
546 biomechanical mechanisms in mouse models: practical guidelines for systematically
547 evaluating phenotypic changes in the diaphyses of long bones. *J Bone Miner Res* **30** 951-
548 966.

549 Judex S, Luu YK, Ozcivici E, Adler B, Lublinsky S & Rubin CT 2010 Quantification of
550 adiposity in small rodents using micro-CT. *Methods* **50** 14-19.
551 Kasugai S, Fujisawa R, Waki Y, Miyamoto K & Ohya K 2000 Selective drug delivery system
552 to bone: small peptide (Asp)6 conjugation. *J Bone Miner Res* **15** 936-943.
553 Mabilleau G, Chappard D & Sabokbar A 2011 Role of the A20-TRAF6 axis in
554 lipopolysaccharide-mediated osteoclastogenesis. *J Biol Chem* **286** 3242-3249.
555 Mabilleau G, Mieczkowska A, Irwin N, Flatt PR & Chappard D 2013 Optimal bone
556 mechanical and material properties require a functional glucagon-like peptide-1 receptor. *J*
557 *Endocrinol* **219** 59-68.
558 Mabilleau G, Mieczkowska A, Irwin N, Simon Y, Audran M, Flatt PR & Chappard D 2014
559 Beneficial effects of a N-terminally modified GIP agonist on tissue-level bone material
560 properties. *Bone* **63** 61-68.
561 Mabilleau G, Perrot R, Mieczkowska A, Boni S, Flatt PR, Irwin N & Chappard D 2016
562 Glucose-dependent insulinotropic polypeptide (GIP) dose-dependently reduces osteoclast
563 differentiation and resorption. *Bone* **91** 102-112.
564 Manhart S, Hinke SA, McIntosh CH, Pederson RA & Demuth HU 2003 Structure-function
565 analysis of a series of novel GIP analogues containing different helical length linkers.
566 *Biochemistry* **42** 3081-3088.
567 Mansur SA, Mieczkowska A, Bouvard B, Flatt PR, Chappard D, Irwin N & Mabilleau G 2015
568 Stable Incretin Mimetics Counter Rapid Deterioration of Bone Quality in Type 1 Diabetes
569 Mellitus. *J Cell Physiol* **230** 3009-3018.
570 Mansur SA, Mieczkowska A, Flatt PR, Bouvard B, Chappard D, Irwin N & Mabilleau G 2016
571 A new stable GIP-Oxyntomodulin hybrid peptide improved bone strength both at the organ
572 and tissue levels in genetically-inherited type 2 diabetes mellitus. *Bone* **87** 102-113.
573 Mieczkowska A, Bouvard B, Chappard D & Mabilleau G 2015a Glucose-dependent
574 insulinotropic polypeptide (GIP) directly affects collagen fibril diameter and collagen cross-
575 linking in osteoblast cultures. *Bone* **74** 29-36.

576 Mieczkowska A, Irwin N, Flatt PR, Chappard D & Mabilleau G 2013 Glucose-dependent
577 insulinotropic polypeptide (GIP) receptor deletion leads to reduced bone strength and quality.
578 *Bone* **56** 337-342.
579 Mieczkowska A, Mansur S, Bouvard B, Flatt PR, Thorens B, Irwin N, Chappard D &
580 Mabilleau G 2015b Double incretin receptor knock-out (DIRKO) mice present with alterations
581 of trabecular and cortical micromorphology and bone strength. *Osteoporos Int* **26** 209-218.
582 Miller SC, Pan H, Wang D, Bowman BM, Kopeckova P & Kopecek J 2008 Feasibility of using
583 a bone-targeted, macromolecular delivery system coupled with prostaglandin E(1) to
584 promote bone formation in aged, estrogen-deficient rats. *Pharm Res* **25** 2889-2895.
585 Montano AM, Oikawa H, Tomatsu S, Nishioka T, Vogler C, Gutierrez MA, Oguma T, Tan Y,
586 Grubb JH, Dung VC, et al. 2008 Acidic amino acid tag enhances response to enzyme
587 replacement in mucopolysaccharidosis type VII mice. *Mol Genet Metab* **94** 178-189.
588 Murphy MB, Hartgerink JD, Goepferich A & Mikos AG 2007 Synthesis and in vitro
589 hydroxyapatite binding of peptides conjugated to calcium-binding moieties.
590 *Biomacromolecules* **8** 2237-2243.
591 Nishioka T, Tomatsu S, Gutierrez MA, Miyamoto K, Trandafirescu GG, Lopez PL, Grubb JH,
592 Kanai R, Kobayashi H, Yamaguchi S, et al. 2006 Enhancement of drug delivery to bone:
593 characterization of human tissue-nonspecific alkaline phosphatase tagged with an acidic
594 oligopeptide. *Mol Genet Metab* **88** 244-255.
595 Nissen A, Christensen M, Knop FK, Vilsboll T, Holst JJ & Hartmann B 2014 Glucose-
596 dependent insulinotropic polypeptide inhibits bone resorption in humans. *J Clin Endocrinol*
597 *Metab* **99** E2325-2329.
598 Oldberg A, Franzen A & Heinegard D 1986 Cloning and sequence analysis of rat bone
599 sialoprotein (osteopontin) cDNA reveals an Arg-Gly-Asp cell-binding sequence. *Proc Natl*
600 *Acad Sci U S A* **83** 8819-8823.
601 Oliver WC & Pharr GM 1992 An improved technique for determining hardness and elastic
602 modulus using load and displacement sensing indentation experiments. *J Mater Res* **7** 1564-
603 1583.

604 Paschalis EP, DiCarlo E, Betts F, Sherman P, Mendelsohn R & Boskey AL 1996 FTIR
605 microspectroscopic analysis of human osteonal bone. *Calcif Tissue Int* **59** 480-487.
606 Paschalis EP, Verdelis K, Doty SB, Boskey AL, Mendelsohn R & Yamauchi M 2001
607 Spectroscopic characterization of collagen cross-links in bone. *J Bone Miner Res* **16** 1821-
608 1828.
609 Pereira M, Gohin S, Roux JP, Fisher A, Cleasby ME, Mabilleau G & Chenu C 2017
610 Exenatide Improves Bone Quality in a Murine Model of Genetically Inherited Type 2 Diabetes
611 Mellitus. *Front Endocrinol (Lausanne)* **8** 327.
612 Rey C, Collins B, Goehl T, Dickson IR & Glimcher MJ 1989 The carbonate environment in
613 bone mineral: a resolution-enhanced Fourier Transform Infrared Spectroscopy Study. *Calcif*
614 *Tissue Int* **45** 157-164.
615 Roschger P, Fratzl P, Eschberger J & Klaushofer K 1998 Validation of quantitative
616 backscattered electron imaging for the measurement of mineral density distribution in human
617 bone biopsies. *Bone* **23** 319-326.
618 Roschger P, Paschalis EP, Fratzl P & Klaushofer K 2008 Bone mineralization density
619 distribution in health and disease. *Bone* **42** 456-466.
620 Shao Y, Hernandez-Buquer S, Childress P, Stayrook KR, Alvarez MB, Davis H, Plotkin LI,
621 He Y, Condon KW, Burr DB, et al. 2017 Improving Combination Osteoporosis Therapy in a
622 Preclinical Model of Heightened Osteoanabolism. *Endocrinology* **158** 2722-2740.
623 Spevak L, Flach CR, Hunter T, Mendelsohn R & Boskey A 2013 Fourier transform infrared
624 spectroscopic imaging parameters describing acid phosphate substitution in biologic
625 hydroxyapatite. *Calcif Tissue Int* **92** 418-428.
626 Takahashi T, Yokogawa K, Sakura N, Nomura M, Kobayashi S & Miyamoto K 2008 Bone-
627 targeting of quinolones conjugated with an acidic oligopeptide. *Pharm Res* **25** 2881-2888.
628 Torekov SS, Harslof T, Rejnmark L, Eiken P, Jensen JB, Herman AP, Hansen T, Pedersen
629 O, Holst JJ & Langdahl BL 2014 A functional amino acid substitution in the glucose-
630 dependent insulinotropic polypeptide receptor (GIPR) gene is associated with lower bone
631 mineral density and increased fracture risk. *J Clin Endocrinol Metab* **99** E729-733.

632 Tsukiyama K, Yamada Y, Yamada C, Harada N, Kawasaki Y, Ogura M, Bessho K, Li M,
633 Amizuka N, Sato M, et al. 2006 Gastric inhibitory polypeptide as an endogenous factor
634 promoting new bone formation after food ingestion. *Mol Endocrinol* **20** 1644-1651.
635 Turner CH & Burr DB 1993 Basic biomechanical measurements of bone: a tutorial. *Bone* **14**
636 595-608.
637 Walsh JS & Henriksen DB 2010 Feeding and bone. *Arch Biochem Biophys* **503** 11-19.
638 Xie D, Cheng H, Hamrick M, Zhong Q, Ding KH, Correa D, Williams S, Mulloy A, Bollag W,
639 Bollag RJ, et al. 2005 Glucose-dependent insulinotropic polypeptide receptor knockout mice
640 have altered bone turnover. *Bone* **37** 759-769.
641 Yokogawa K, Miya K, Sekido T, Higashi Y, Nomura M, Fujisawa R, Morito K, Masamune Y,
642 Waki Y, Kasugai S, et al. 2001 Selective delivery of estradiol to bone by aspartic acid
643 oligopeptide and its effects on ovariectomized mice. *Endocrinology* **142** 1228-1233.

644

FIGURE LEGENDS

Figure 1: Mineral-binding capacity of GIP analogues. (A) 5-FAM-[D-Ala^2]-GIP-Tag and FAM-[D-Ala^2]-GIP$_{1-30}$ were incubated for 24h with disks of pHEMA that had been previously mineralized. 5-FAM and Calcein were used as negative and positive controls, respectively. 5-FAM-[D-Ala^2]-GIP-Tag but not 5-FAM-[D-Ala^2]-GIP$_{1-30}$ was capable of significantly binding to the mineralized disks. Values are means ± SEM. #: $p<0.05$ vs. 5-FAM. (B) Tissue distribution of 5-FAM, 5-FAM-[D-Ala^2]-GIP$_{1-30}$ and 5-FAM-[D-Ala^2]-GIP-Tag. Fluorescence, in arbitrary units (a.u.) was weighted by the protein mass and detected in several tissues harvested from animals injected with 5-FAM-[D-Ala^2]-GIP$_{1-30}$. On the other hand, fluorescence due to 5-FAM-[D-Ala^2]-GIP-Tag was exclusively found in bone. *: $p<0.05$ vs.5-FAM, #: $p<0.05$ vs.5-FAM-[D-Ala^2]-GIP$_{1-30}$. Values are means ± SEM. (C) 5-FAM-[D-Ala^2]-GIP$_{1-30}$ and 5-FAM-[D-Ala^2]-GIP-Tag were injected into young mice and the extent of GIP analogue binding in bone was assessed after 16h. A significant fluorescent line was clearly visible in the bone matrix of animals injected with 5-FAM-[D-Ala^2]-GIP-Tag but not in animals injected with 5-FAM-[D-Ala^2]-GIP$_{1-30}$. Arrowheads indicate the fluorescence line. CtB: cortical bone, BM: bone marrow. (D) [D-Ala²]-GIP-Tag at acidic but not neutral pH was released from the bone slice as demonstrated by significant higher level of fluorescence. *: $p<0.05$ vs. pH 7.0. Values are means ± SEM.

Figure 2: Biological activity of GIP analogues. (A) Receptor binding properties and activation of cAMP and intracellular calcium. Receptor binding properties, cAMP and intracellular calcium responses of [D-Ala^2]-GIP$_{1-30}$ and [D-Ala^2]-GIP-Tag were not significantly different to those of native GIP$_{1-42}$. Values are means ± SEM. (B) Activation of intracellular pathways in MC3T3-E1 cells. [D-Ala^2]-GIP$_{1-30}$, [D-Ala^2]-GIP-Tag and GIP$_{1-42}$ significantly increased the phosphorylation of p38α, CREB, AMPKα2 and STAT2 in a similar manner. *: $p<0.05$ vs. vehicle. Values are means ± SEM. (C) [D-Ala^2]-GIP$_{1-30}$, [D-Ala^2]-GIP-Tag and

GIP_{1-42} significantly increased collagen maturity *in vitro* and (D) reduced the number of newly generated osteoclast per well and the extent of osteoclast resorption. Values are means ± SEM. *: p<0.05 vs. vehicle and #: p<0.05 vs. M-CSF+RANKL.

Figure 3: Effects of GIP analogues on bone strength in ovariectomy-induced bone loss. (A-F) Bone strength has been assessed at the whole body-level by three point bending and (G-J) at the tissue level by nanoindentation. Values are means ± SEM. H_{IT}: indentation hardness, E_{IT}: indentation modulus, Force max: Maximum load to reach 900 nm in depth, W_{plast}: Dissipated energy. *: p<0.05 vs. OVX+Veh.

Figure 4: Effects of GIP analogues on bone matrix composition. (A) Tissue mineral density distribution has been studied by qBEI at the midshaft tibia and revealed significant lower values of Ca_{mean} and Ca_{turn} in the presence of [D-Ala^2]-GIP_{1-30} or [D-Ala^2]-GIP-Tag and a significant lower heterogeneity and higher Ca_{turn} in the presence of alendronate. Values are means ± SEM. *: p<0.05 vs. OVX+Veh. (B) Bone matrix composition has been investigated at site of bone formation and revealed the lack of effects of both GIP analogues. Treatment with alendronate resulted in higher values for carbonate-to-phosphate ratio and type B carbonate substitution and a lower value of labile carbonate substitution. Values are means ± SEM. *: p<0.05 vs. OVX+Veh.

9. TABLES

Table 1. Peptide sequences and characteristics

GIP analogues	Amino acid sequence	Purity	Theoretical molecular weight (Da)	Measured molecular weight (Da)
GIP_{1-42}	Y[D-Ala]EGTFISDYSIAMDKIHQQDFVNWLLAQKGKKNDWKHNITQ	96.5%	4983.53	4983.64
[D-Ala^2]-GIP_{1-30}	Y[D-Ala]EGTFISDYSIAMDKIHQQDFVNWLLAQK	97.9%	3531.95	3532.02
5-FAM-[D-Ala^2]-GIP_{1-30}	5'Fam-Y[D-Ala]EGTFISDYSIAMDKIHQQDFVNWLLAQK	96.9%	3890.25	3890.34
[D-Ala^2]GIP-Tag	Y[D-Ala]EGTFISDYSIAMDKIHQQDFVNWLLAQKGAADDDDDD	95.8%	4421.68	4421.76
5-FAM-[D-Ala^2]GIP-Tag	5'Fam- Y[D-Ala]EGTFISDYSIAMDKIHQQDFVNWLLAQKGAADDDDDD	95.6%	4779.98	4780.08

Table 2. Body weight, composition and metabolic properties.

	Sham+Veh	OVX+Veh	OVX+GIP$_{1-30}$	OVX+GIP-Tag	OVX+Aln
Body mass (g)	23.5 ± 0.4 (0.062)	25.6 ± 0.9	26.1 ± 0.5 (0.945)	23.3 ± 0.6 (0.053)	26.6 ± 0.6 (0.645)
Abdominal fat volume (%)	14.6 ± 0.6 (<0.001)	24.7 ± 2.4	23.1 ± 1.6 (0.695)	10.8 ± 1.0 (<0.001)	25.6 ± 1.8 (0.695)
Uterus mass (g)	0.14 ± 0.01 (<0.001)	0.04 ± 0.01	0.05 ± 0.01 (0.915)	0.03 ± 0.01 (0.674)	0.05 ± 0.01 (0.915)
Femur length (mm)	13.9 ± 0.1 (0.967)	14.0 ± 0.1	14.1 ± 0.1 (0.980)	14.0 ± 0.1 (0.999)	14.2 ± 0.1 (0.898)
Marrow adipose tissue (%)	0.6 ± 0.2 (0.498)	1.0 ± 0.4	0.4 ± 0.1 (0.123)	0.2 ± 0.1 (0.043)	1.2 ± 0.2 (0.960)
Non fasting glucose (mmol/l)	9.7 ± 0.4 (0.574))	10.5 ± 0.6	10.6 ± 0.6 (>0.999)	10.7 ± 0.3 (0.627)	10.6 ± 0.3 (>0.999)
CTx-I (ng/ml)	8.9 ± 0.5 (<0.001)	14.7 ± 1.0	9.2 ± 0.7 (<0.001)	9.4 ± 1.0 (0.02)	10.8 ± 1.0 (<0.001)
P1NP (ng/ml)	20.4 ± 1.7 (0.062)	26.4 ± 1.3	23.6 ± 1.9 (0.680)	21.3 ± 2.1 (0.120)	22.5 ± 1.3 (0.340)

Data are presented as mean ± SEM (p value). Data have been analyzed by one-way ANOVA followed by *post hoc* Dunnett's multiple comparison test using OVX+Veh group as the control group. Bold values represent significant differences as compared with OVX+Veh. CTx-I: C-terminal telopeptide of type I collagen, P1NP: N-terminal propeptide of type I procollagen.

Table 3. Cortical bone microarchitectural parameters at the midshaft tibia.

	Sham+Veh	OVX+Veh	OVX+GIP_{1-30}	OVX+GIP-Tag	OVX+Aln
Tt.Ar (mm^2)	1.72 ± 0.04 (0.025)	1.54 ± 0.04	1.70 ± 0.03 (0.042)	1.66 ± 0.03 (0.221)	1.51 ± 0.08 (0.988)
Ma.Ar (mm^2)	0.71 ± 0.02 (0.005)	0.61 ± 0.02	0.71 ± 0.01 (0.004)	0.67 ± 0.01 (0.208)	0.63 ± 0.03 (0.873)
Ct.Ar (mm^2)	1.00 ± 0.02 (0.038)	0.90 ± 0.01	0.98 ± 0.02 (0.044)	0.96 ± 0.03 (0.378)	0.87 ± 0.05 (0.747)
Ct.Th (μm)	245 ± 3 (0.411)	236 ± 5	230 ± 5 (0.630)	235 ± 4 (0.997)	225 ± 6 (0.740)
Iap (mm^4)	0.23 ± 0.01 (0.814)	0.22 ± 0.02	0.24 ± 0.01 (0.538)	0.22 ± 0.01 (0.990)	0.24 ± 0.03 (0.815)
Iml (mm^4)	0.26 ± 0.00 (0.648)	0.24 ± 0.01	0.27 ± 0.01 (0.297)	0.28 ± 0.01 (0.081)	0.19 ± 0.02 (0.028)
J (mm^4)	0.49 ± 0.03 (0.347)	0.44 ± 0.02	0.52 ± 0.01 (0.049)	0.48 ± 0.02 (0.648)	0.41 ± 0.04 (0.800)

Data are presented as mean ± SEM (p value). Data have been body-size adjusted with a linear regression method and analyzed by one-way ANOVA followed by *post hoc* Dunnett's multiple comparison test using OVX+Veh group as the control group. Bold values represent significant differences as compared with OVX+Veh. Tt.Ar: total cross-sectional area, Ma.Ar: medullary area, Ct.Ar: cortical bone area, Ct.Th: cortical thickness, Iap: moment of inertia about the anteroposterior axis, Iml: moment of inertia about the mediolateral axis, J: polar moment of inertia

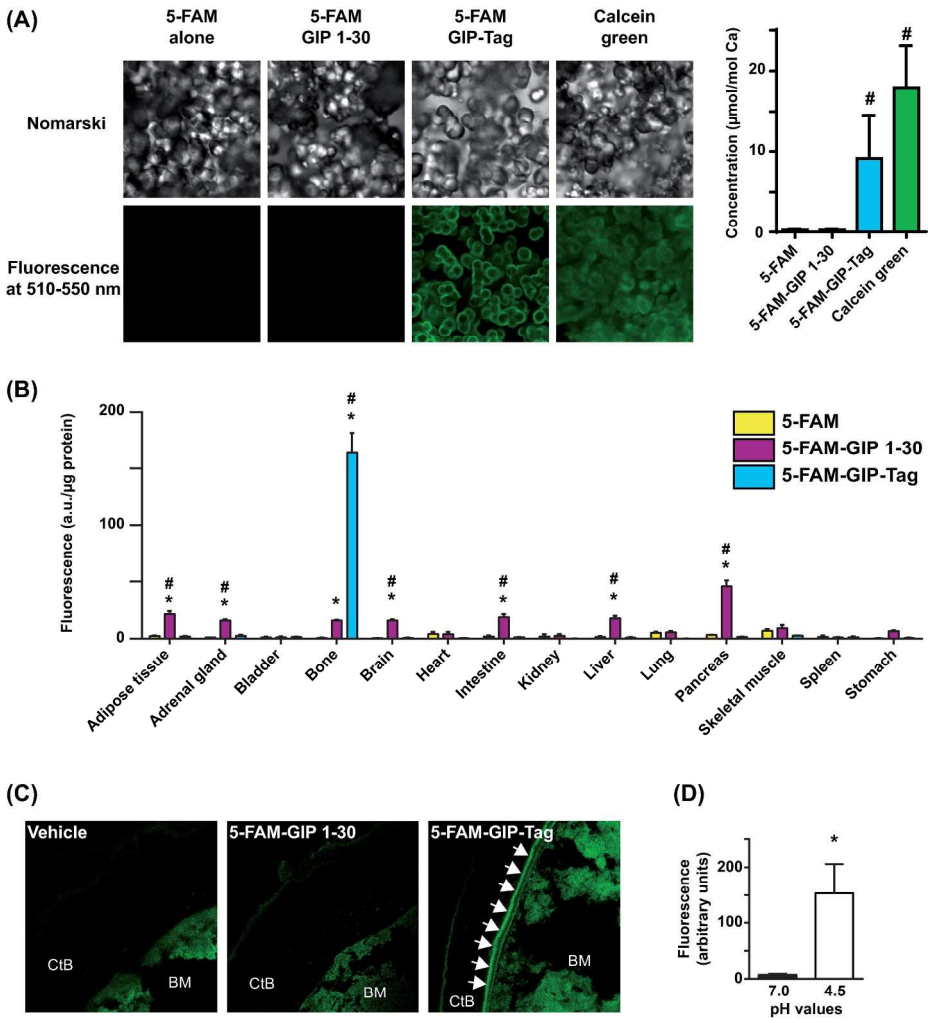

Figure 1

219x285mm (300 x 300 DPI)

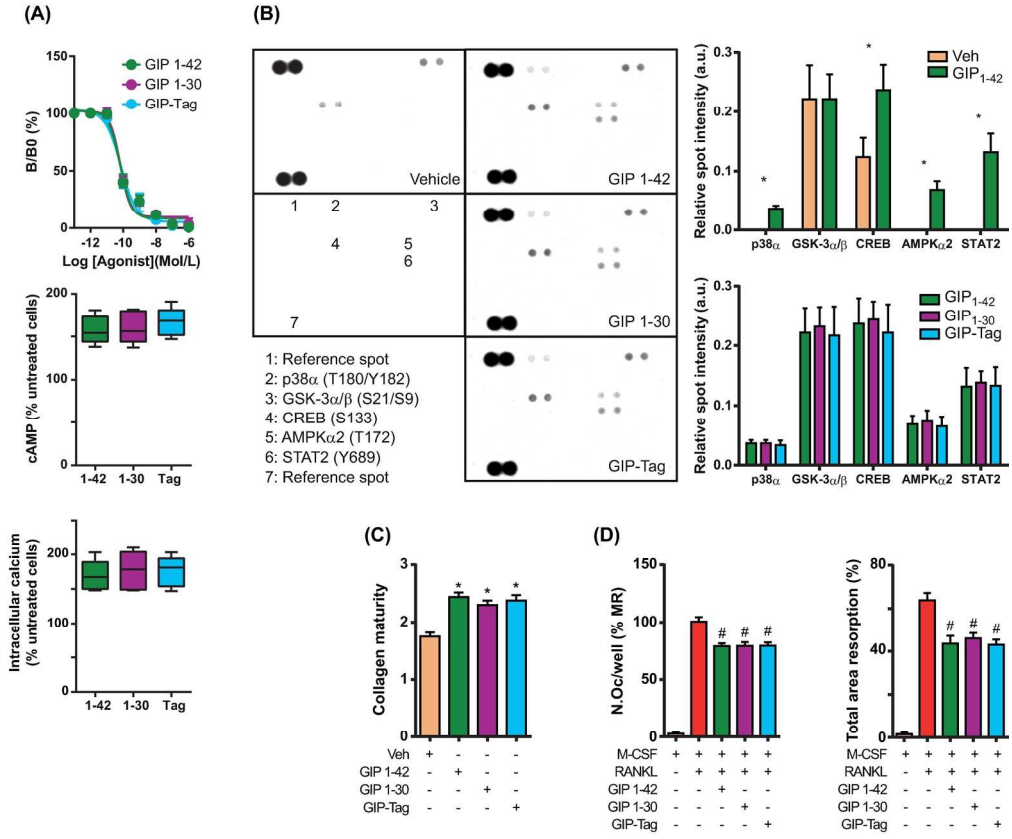

Figure 2

185x192mm (300 x 300 DPI)

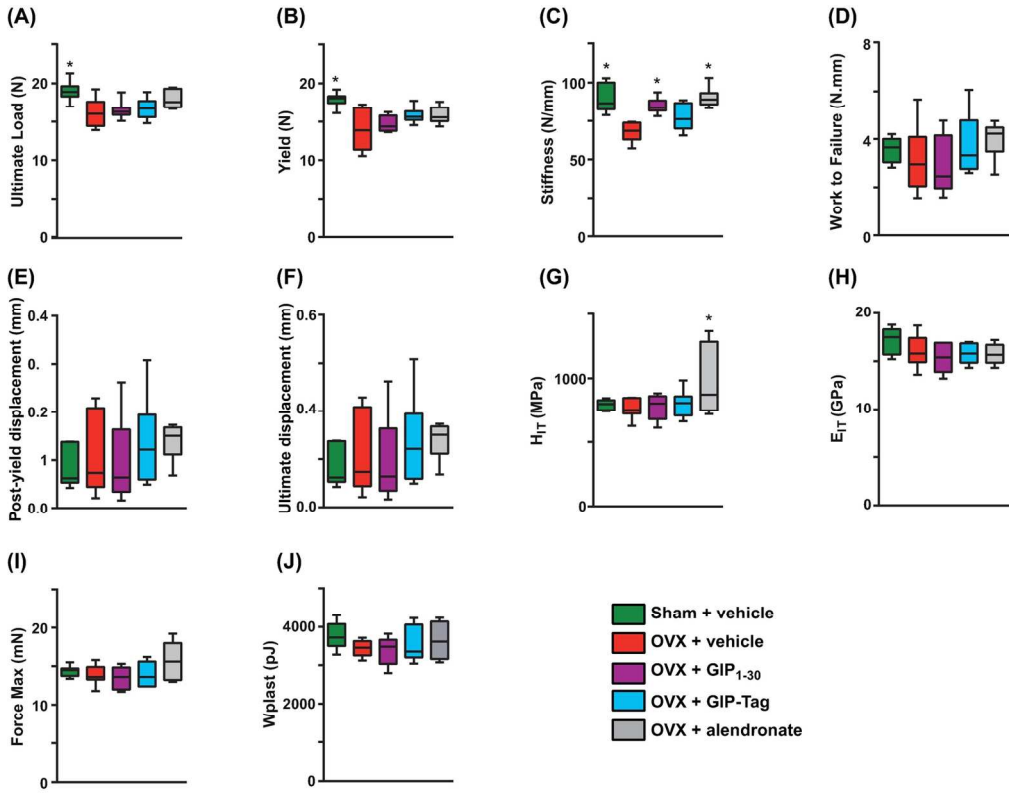

Figure 3

150x137mm (300 x 300 DPI)

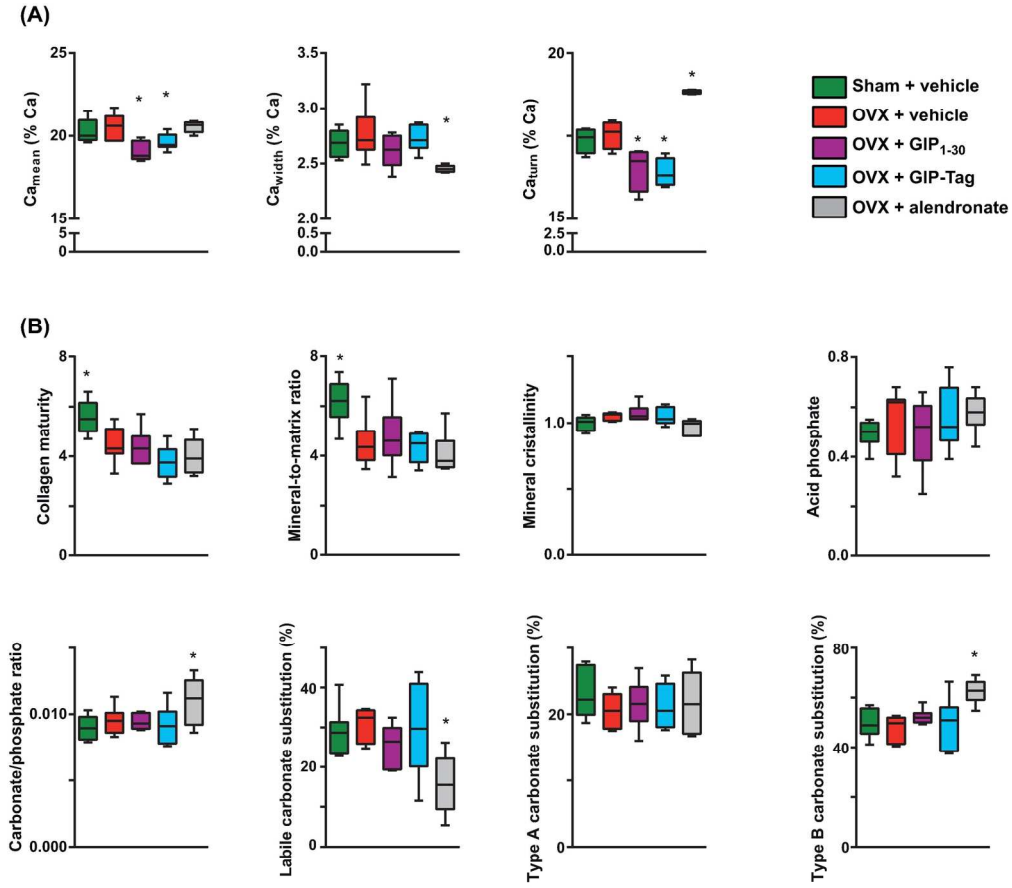

Figure 4

171x183mm (300 x 300 DPI)